Extreme sensitivity of the magnetic ground state to halide composition in $FeCl_{3-x}Br_x$

Andrew Cole,[1] Alenna Streeter,[1] Adolfo O. Fumega,[2] Xiaohan Yao,[1] Zhi-Cheng Wang,[1] Erxi Feng,[3] Huibo Cao,[3] Jose L. Lado,[2] Stephen E. Nagler,[3] and Fazel Tafti[1]

[1]*Department of Physics, Boston College, Chestnut Hill, Massachusetts 02467, USA*

[2]*Department of Applied Physics, Aalto University, Espoo 02150, Finland*

[3]*Neutron Scattering Division, Oak Ridge National Laboratory, Oak Ridge, Tennessee 37831, USA*

(Received 27 March 2023; accepted 12 May 2023; published 2 June 2023)

Mixed halide chemistry has recently been utilized to tune the intrinsic magnetic properties of transition-metal halides—one of the largest families of magnetic van der Waals materials. Prior studies have shown that the strength of exchange interactions, hence the critical temperature, can be tuned smoothly with halide composition for a given ground state. Here we show that the ground state itself can be altered by a small change of halide composition in $FeCl_{3-x}Br_x$. Specifically, we find a threefold jump in the Néel temperature and a sign change in the Weiss temperature at $x = 0.08$ corresponding to only 3% bromine doping. Using neutron scattering, we reveal a change of the ground state from spiral order in $FeCl_3$ to *A*-type antiferromagnetic order in $FeBr_3$. From first-principles calculations, we show that a delicate balance between nearest and next-nearest neighbor interactions is responsible for such a transition. These results demonstrate how varying the halide composition can tune the competing interactions and change the ground state of a spiral spin liquid system.

DOI: 10.1103/PhysRevMaterials.7.064401

I. INTRODUCTION

Magnetic frustration provides a fascinating playground for the realization of exotic quantum states [1]. A curious example of frustrated magnet is the spiral spin-liquid (SSL) phase produced by competing interactions in a bipartite lattice such as diamond (3D) and honeycomb (2D) structures. The SSL is characterized by degenerate spin spirals with **k** vectors lying on a surface in momentum space [2]. Weak thermal fluctuations can entropically lift this degeneracy and establish order by disorder [3]. Spinel materials such as $MnSc_2S_4$ and $CoAl_2O_4$ are candidates of SSL in the 3D diamond lattice described by a frustrated J_1-J_2 Heisenberg model [4–8]. In 2D, however, the experimental realization of such effects in the honeycomb lattice [9,10], prevalent in van der Waals (VdW) materials, has remained elusive.

Recent neutron scattering experiments on the VdW magnet $FeCl_3$ with a honeycomb lattice have shown a ring of degenerate **k** vectors just above $T_N = 8.5$ K, indicating a 2D SSL phase [11]. Below T_N, a spiral order with $\mathbf{k} = (\frac{4}{15}, \frac{1}{15}, \frac{3}{2})$ is established [12,13] indicating the entropic selection of this propagation vector by spin fluctuations, i.e., order by disorder.

In this article, we reveal the extreme sensitivity of the ground state of $FeCl_3$ to tiny amounts of disorder by characterizing a series of $FeCl_{3-x}Br_x$ crystals [Figs. 1(a)–1(c)]. We find a threefold jump in the Néel temperature (T_N) and a sign change in the Weiss temperature (Θ_W) between $x = 0$ and 0.08 corresponding to only 3% bromine doping. Such dramatic enhancement of the order due to a tiny amount of disorder suggests that $FeCl_3$ is a frustrated magnet on the verge of a change of the ground state from the SSL to a different ordered state [Fig. 1(d)]. For $x \geqslant 0.08$, we identify the ordered state to be *A*-type AFM, which is ferromagnetic (FM) within the layers and AFM between them. This is similar to the ground state of $FeBr_3$ and different from the spiral order in $FeCl_3$.

Our experimental results are corroborated by first-principles calculations on a 2D J_1-J_2 Heisenberg model that predict a change of the ground state from the SSL to FM in $FeCl_{3-x}Br_x$ as observed experimentally. We discuss the importance of including *p*-orbital correlations, in addition to *d*-orbital correlations, for obtaining the correct magnetic ground state in density functional theory (DFT). To our knowledge, the impact of *p*-orbital correlations in DFT calculations for VdW materials has not been discussed in the literature before. Details of crystal growth, neutron scattering, scanning electron microscopy (SEM), magnetization measurements, and DFT calculations are explained in the Supplemental Material [14] that includes additional references [15–24].

II. RESULTS AND DISCUSSION

Among different classes of VdW magnets, transition-metal halides offer a special opportunity in that their intrinsic properties can be tuned by mixing the halide species (Cl, Br, and I) [25]. With increasing halide size, the orbital overlaps and ligand spin-orbit coupling (SOC) are enhanced, which in turn tune all magneto-optical properties as reported previously in $CrCl_{3-x}Br_x$, $CrBr_{3-y}I_y$, and $CrCl_{3-x-y}Br_xI_y$ alloys [25,26].

Following the recent report of a SSL ground state and order by disorder in $FeCl_3$ [11], we grew the mixed-halide crystals of $FeCl_{3-x}Br_x$ with the goal of tuning the SSL ground state. Since both $FeCl_3$ and $FeBr_3$ crystallize in the rhombohedral space group $R\bar{3}m$ with a layered honeycomb structure, a solid solution of $FeCl_{3-x}Br_x$ crystals can also be grown with the same structure [Figs. 1(a) and 1(b)]. The composition and uniform distribution of elements were confirmed using

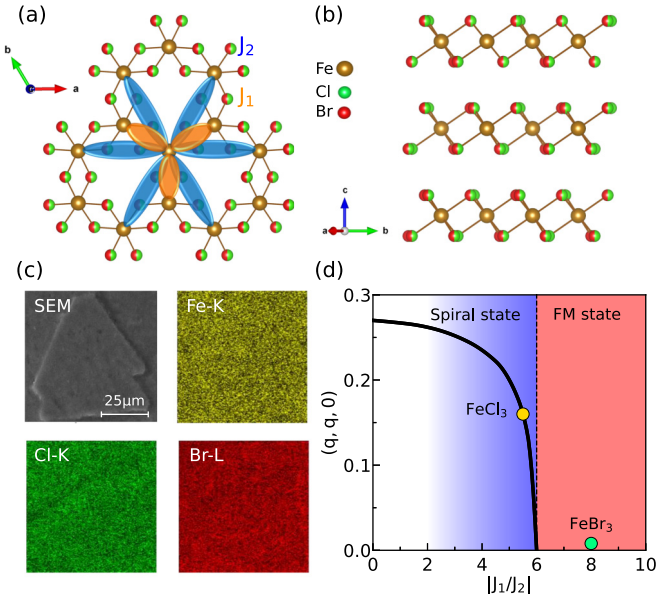

FIG. 1. (a) Schematic illustration of the honeycomb *ab* planes in the mixed halide system $FeCl_{1.5}Br_{1.5}$. The J_1 and J_2 exchange paths are highlighted in orange and blue colors, respectively. (b) Layered (VdW) structure of $FeCl_{1.5}Br_{1.5}$ viewed from the [210] direction. (c) SEM image and EDX color maps confirming the homogeneous distribution of halides in an $FeCl_{1.33}Br_{1.67}$ crystal. (d) Phase diagram of the spiral and FM states with $FeCl_3$ and $FeBr_3$ across the phase boundary. Here, the $(q, q, 0)$ y label is the degenerate magnetic wave vector for the SSL state, not the final spiral ground state [11]. $FeBr_3$ is not in the SSL phase and its order is FM in 2D.

energy dispersive x-ray spectroscopy (EDX). For example, Fig. 1(c) shows the distribution of Fe K-edge (yellow), Cl K-edge (green), and Br L-edge (red) absorption intensities in $FeCl_{1.33}Br_{1.67}$.

The superexchange interactions between Fe^{3+} ions are mediated by Cl and Br ligands within the honeycomb layers of each $FeCl_{3-x}Br_x$ sample. The nearest neighbor (NN) and next-nearest neighbor (NNN) exchange paths are denoted by J_1 and J_2 in Fig. 1(a), respectively. Although J_2 is weaker than J_1, there are six NNNs and three NNs, leading to a close competition between the J_1 and J_2 terms in the model Hamiltonian

$$H = J_1 \sum_{\langle ij \rangle} \vec{S}_i \cdot \vec{S}_j + J_2 \sum_{\langle\langle ij \rangle\rangle} \vec{S}_i \cdot \vec{S}_j, \qquad (1)$$

where $S = 5/2$ in the high-spin state of Fe^{3+} ($^6S_{5/2}$). The competition between different magnetic exchange paths (direct and superexchange) leads to effective $J_1 < 0$ (FM) and $J_2 > 0$ (AFM) for the 2D spin model of Eq. (1). The ratio between J_1 and J_2, $|J_1/J_2|$, determines the magnetic ground state of the honeycomb lattice as well as the degenerate $(q, q, 0)$ wave vector of the SSL phase above T_N which is shown schematically in Fig. 1(d). It is known from prior neutron diffraction experiments [12] that the ground state of $FeCl_3$ is a spin spiral. We will show here that the Br substitution modifies the $|J_1/J_2|$ ratio and drives the system to an A-type AFM state (which is FM in 2D), where $FeBr_3$ is located in Fig. 1(d).

A. Magnetization measurements

The experimental evidence of competing FM and AFM interactions appear in the magnetic susceptibility (χ) and magnetization (M) data. The raw data for all samples with $H \| c$ and $H \perp c$ are shown in Figs. 2(a)–2(d) and the analyzed results are presented in Figs. 2(e)–2(h). The empty and full circles in Figs. 2(a) and 2(b) correspond to zero-field-cooled (ZFC) and field-cooled (FC) measurements, respectively. In Fig. 2(a), the peaks in $\chi(T)$ curves with $H \| c$ and the minimal difference between the ZFC and FC curves are characteristics of AFM transitions. Unlike $H \| c$, the $H \perp c$ curves in Fig. 2(b) do not go to zero when $T \to 0$, indicating a finite FM component. A combination of FM and AFM correlations also exists in $CrCl_3$, which undergoes an A-type AFM order (FM within the layers and AFM between them) [27]. In $CrCl_3$, only the t_{2g} manifold of Cr^{3+} is at half filling, whereas both t_{2g} and e_g levels are at half filling in $FeCl_3$, maximizing the competition between FM and AFM correlations according to Goodenough-Kanamori rules [28,29].

We determined T_N from $d\chi/dT$ curves (Supplemental Fig. S1) [14] and plotted it as a function of bromine content (x in $FeCl_{3-x}Br_x$) for both field directions in Fig. 2(e). Using a Curie-Weiss (CW) analysis (Supplemental Fig. S1) [14], we extracted Θ_W, which is a rough measure of the magnetic correlations, and plotted it as a function of x in Fig. 2(f). The central observation in Figs. 2(e) and 2(f) is a jump in both T_N and Θ_W when a tiny amount of Br is added to $FeCl_3$, i.e., at $x = 0.08$ in $FeCl_{3-x}Br_x$ corresponding to only 3% Br doping. The effect is dramatic, with T_N showing a threefold jump and Θ_W changing sign, indicating a change of magnetic ground state at $x = 0.08$. From the CW analysis, we found the effective magnetic moment of all $FeCl_{3-x}Br_x$ samples to be close to 5.9 μ_B within experimental errors [Fig. 2(g)] as expected for Fe^{3+} in the high-spin state.

After the initial threefold jump of T_N from 8.5(2) K at $x = 0$ to 23.1(1) K at $x = 0.08$, it is suppressed linearly to 14.5(5) K at $x = 3$ [Fig. 2(e)]. This behavior is the same for both field directions. Similarly, after the initial jump of Θ_W from -13 K at $x = 0$ to $+21$ K at $x = 0.08$, it is suppressed linearly to 8 K at $x = 3$ for both field directions [Fig. 2(f)]. Two conclusions can be drawn from these observations. (i) The initial jump in T_N and sign change in Θ_W suggest an abrupt change of the magnetic ground state of $FeCl_3$ by a tiny amount in Br doping. (ii) The linear decrease of both T_N and Θ_W from $x = 0.08$ to 3 suggests that the ground states of all $FeCl_{3-x}Br_x$ samples with $x \geqslant 0.08$ are similar to the ground state of $FeBr_3$ and different from that of $FeCl_3$.

Another evidence for the change of the magnetic ground state at $x = 0.08$ comes from the field dependence of magnetization. The $M(H)$ curves of $FeCl_3$ in Figs. 2(c) and 2(d) are nearly linear in both field directions, consistent with the spiral AFM order reported in prior neutron diffraction studies [12]. The subtle kinks in the $M(H \perp c)$ curves at $H = 0$ and 4 T in $FeCl_3$ are due to the alignment of spiral domains with the field [12]. Unlike $FeCl_3$, the $FeCl_{3-x}Br_x$ samples with $x \geqslant 0.08$ exhibit field-induced metamagnetic (MM) transitions when $H \| c$ and linear $M(H)$ when $H \perp c$ [Figs. 2(c) and 2(d)]. Tracing the critical field (H_c) of the MM transition as a function of x [Fig. 2(h)] reveals an initial jump at $x = 0.08$ followed

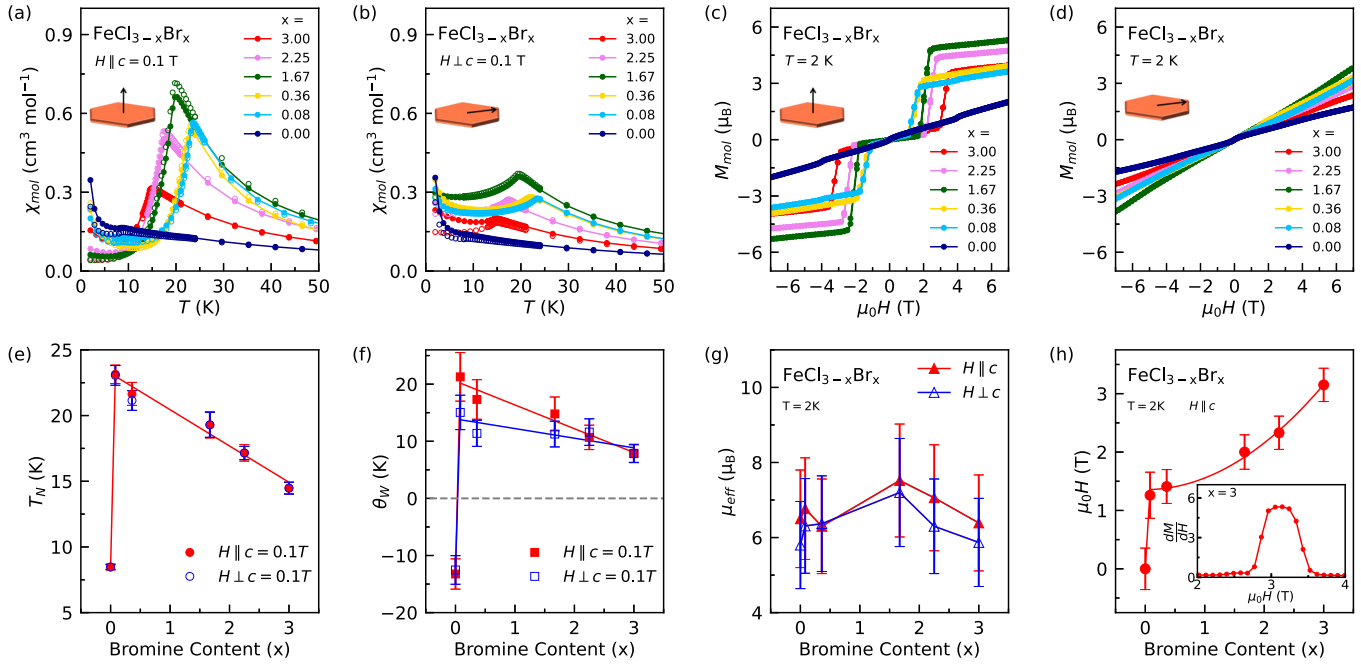

FIG. 2. (a) Magnetic susceptibility as a function of temperature measured under ZFC (open circles) and FC (full circles) conditions with $H \| c$. (b) Same as in (a) but with $H \perp c$. (c) Magnetization curves with $H \| c$ showing metamagnetic (MM) transitions in $FeCl_{3-x}Br_x$ samples with $x \geqslant 0.08$. (d) The MM transitions are absent when $H \perp c$. (e) T_N as a function of Br content (x) showing an initial jump followed by a linear decrease. (f) Θ_W as a function of x showing an initial sign change followed by a linear decrease. (g) μ_{eff} estimated from the Curie-Weiss analysis (Fig. S1). Error bars in panels (e), (f), and (g) are mainly due to the uncertainty in evaluating the mass of thin VdW crystals. (h) The critical field of MM transitions as a function of x showing an initial jump followed by a smooth increase. Error bars reflect the width of the transition (inset).

by a smooth increase of H_c for $x \geqslant 0.08$. The H_c values in Fig. 2(h) correspond to the peak fields in the dM/dH curves shown in the inset. Similar to the behavior of T_N and Θ_W [Figs. 2(e) and 2(f)], the initial jump of H_c at $x = 0.08$ in Fig. 2(h) indicates a change of the magnetic ground state and its subsequent smooth increase indicates that the ground states of $FeCl_{3-x}Br_x$ samples with $x \geqslant 0.08$ are similar to that of $FeBr_3$ and different from $FeCl_3$.

B. Neutron diffraction

Single crystal neutron diffraction has been performed on $FeCl_3$ previously and the ground state was determined as AFM with a spiral modulation parallel to the $[14\bar{5}]$ direction with a wavelength of 15 $(14\bar{5})$ d spacing [12]. We performed single-crystal neutron diffraction on $FeBr_3$ at 4.8 K and zero field to probe its magnetic ground state. Since all $FeCl_{3-x}Br_x$ samples with $x \neq 0$ have similar $\chi(T)$ and $M(H)$ behaviors as $FeBr_3$ (Fig. 2), we assume that their magnetic ground states are similar to that of $FeBr_3$.

The observed Bragg peaks in Figs. 3(a) and 3(b) at $\mathbf{Q} = (2, \bar{1}, L)$ consist of structural (nuclear) peaks at $L = 3$ and 6, as well as magnetic peaks at $L = \frac{3}{2}$, $3 + \frac{3}{2}$, and $6 + \frac{3}{2}$; hence the magnetic propagation vector $\mathbf{k} = (0, 0, 1.5)$. The systematic absence of the nuclear peaks other than $L = 3n$ ($n \in$ integer) in Figs. 3(a) and 3(b) is expected in the space group $R\bar{3}$ (no. 148) of $FeBr_3$. A second scan along $\mathbf{Q} = (1, \bar{1}, L)$ in Figs. 3(c) and 3(d) confirms the propagation vector $\mathbf{k} = (0, 0, 1.5)$. The absence of magnetic reflections at $\mathbf{Q} = (0, 0, L)$ (i.e., $L = 4.5$ and 7.5) in Fig. 3(e) suggests that the ordered magnetic moments lie along the c axis because neutrons probe the moment perpendicular to scattering vector ($\mathbf{M} \perp \mathbf{Q}$). Thus we identify $FeBr_3$ as an Ising system with moments pointing out of plane ($M_z \neq 0$ and $M_{x,y} = 0$).

We construct an order parameter plot in Fig. 3(f) by tracing the intensity of the $\mathbf{Q} = (2, \bar{1}, 4.5)$ peak as a function of temperature. From a power-law fit, we extract $T_N = 14.0(5)$ K consistent with 14.5(5) K from the magnetization measurements and $\beta = 0.324(15)$ consistent with a 3D Ising system.

A magnetic symmetry analysis based on the ordering wave vector $\mathbf{k} = (0, 0, 1.5)$ for $S = 5/2$ Fe^{3+} ions in the structural space group $R\bar{3}$ of $FeBr_3$ identifies six possible ground states. These states are labeled in Figs. 3(g)–3(l) by their magnetic subgroups and irreducible representations (irreps) as $R_l\bar{3}$ (irrep: mT_1^+), $R_l\bar{3}$ (mT_1^-), R_l3 (mT_1^+), $P_s\bar{1}$ (mT_1^+), $P_s\bar{1}$ (mT_1^-), and P_s1 (mT_1^+). The first two candidates in Figs. 3(g) and 3(h) represent maximal symmetry subgroups corresponding to an Ising system with moments pointing out of plane ($M_z \neq 0$ and $M_{x,y} = 0$) in an A-type and C-type AFM state, respectively. The lower symmetry R_l3 similarly allows only M_z components but with two different moment sizes [Fig. 3(i)]. The later three subgroups [Figs. 3(j), 3(k), and 3(l)] are primitive (P) instead of rhombohedral (R). Having a lower symmetry, they allow for each of the previous cases in Figs. 3(g), 3(h), and 3(i) to have moments canted toward the ab plane, i.e., $M_{x,y} \neq 0$.

We identify the ground state of $FeBr_3$ as an A-type AFM order [Fig. 3(g)] for the following reasons. (i) The lack of magnetic reflections along the $00L$ direction in Fig. 3(e) indicates that the allowed magnetic moments lie along the c axis, which disqualifies the configurations in Figs. 3(j), 3(k), and

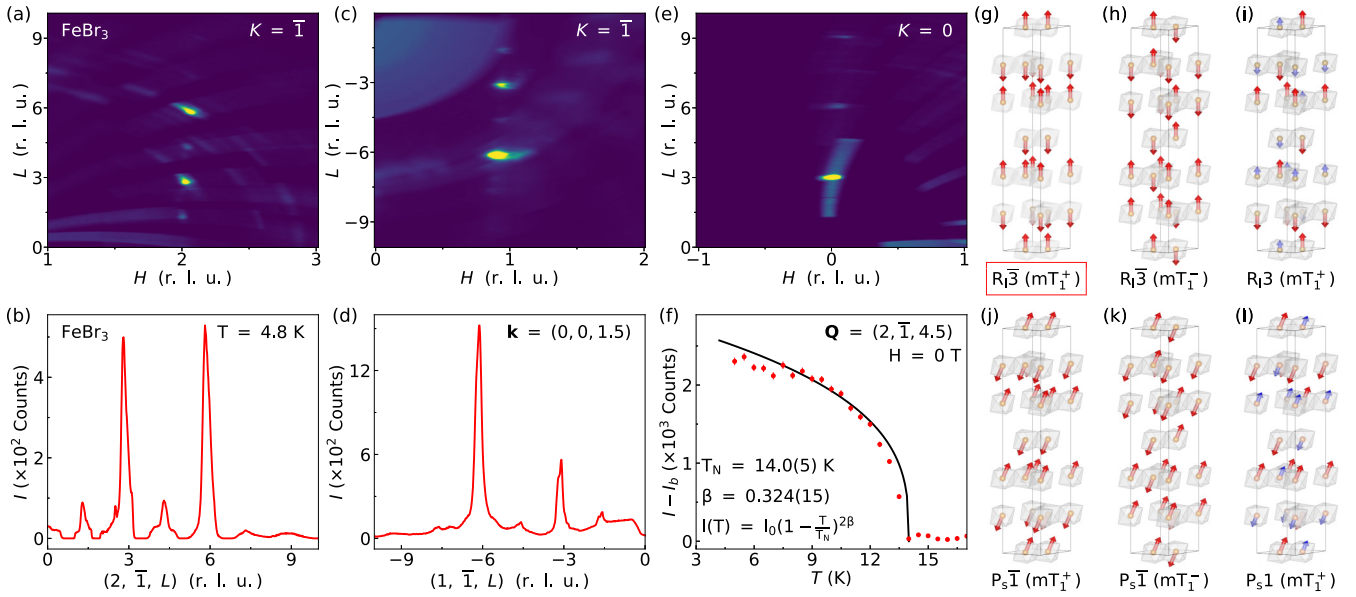

FIG. 3. (a) 2D neutron diffraction scan at 4.8 K and zero field in the H-L plane at $K = \bar{1}$, showing strong nuclear reflections at integer L and weak magnetic reflections at half-integer L. (b) A 1D cut through the data in panel (a) showing nuclear (strong) and magnetic (weak) Bragg peaks that identify the magnetic propagation vector $\mathbf{k} = (0, 0, 1.5)$. (c) 2D scan in the $(H\bar{1}L)$ plane showing another set of nuclear and magnetic reflections. (d) 1D cut through the data in panel (c) showing Bragg peaks along $(1\bar{1}L)$ direction. (e) 2D scan in the $(H0L)$ plane showing the absence of magnetic reflections along the $(00L)$ direction. (f) Temperature dependence of the intensity of the magnetic reflection $\mathbf{Q} = (2, \bar{1}, 4.5)$ with a power-law fit to extract T_N and the critical exponent β. (g),(h),(i) Candidate magnetic ground states of $FeBr_3$ with R_l symmetry. (j),(k),(l) Candidate ground states with P_s symmetry. The ground state is determined as A-type AFM shown in panel (g).

3(l) with allowed moments in the *ab* plane. (ii) Our neutron scattering refinement of the magnetic moment size (SI) gives 4.90(99) μ_B on each Fe^{3+} site, consistent with the results of magnetization measurements and slightly larger than the 4.3 μ_B reported for $FeCl_3$ in prior studies [12,13]. Thus the configuration in Fig. 3(i) with different moment sizes on different Fe sites is also disqualified. (iii) The remaining candidates in Figs. 3(g) and 3(h) belong to the maximal subgroup $R_l\bar{3}$ corresponding to the A-type and C-type AFM ordering, respectively. These two structures can be distinguished according to the intensity of magnetic diffraction peaks. We simulated the structure factor (F^2_{sim}) for several nuclear and magnetic Bragg peaks in both A-type and C-type structures assuming $\mu = 4.9\,\mu_B$ and summarized them in the Supplemental Table I [14]. According to Table I, F^2_{sim} values for two magnetic Bragg peaks are vanishingly small in the C-type AFM structure and considerably large in the A-type AFM structure. Thus the diffraction pattern is best described by A-type AFM ordering [Fig. 3(g)].

An A-type AFM ground state is also consistent with the field scale of the MM transition in Fig. 2(c), which is about 3 T in $FeBr_3$ corresponding to 2 K (using $\mu_B H \sim k_B T$), considerably smaller than $T_N = 14$ K. Thus the MM transitions are likely due to a spin flip between the layers instead of within the layers, so the ground state must be A-type instead of C-type AFM.

C. First-principles calculations

Our experimental results demonstrate a change of the magnetic ground state from the spiral order in $FeCl_3$ to an A-type AFM order upon 3% bromine doping ($x = 0.08$ in $FeCl_{3-x}Br_x$). To understand the nature of the transition, we performed all-electron first-principles calculations based on DFT in $FeCl_3$ and $FeBr_3$ to extract J_1 and J_2 exchange couplings in the model Hamiltonian Eq. (1) for a 2D honeycomb lattice of $S = 5/2$ spins [Fig. 1(a)]. We extracted J_1 and J_2 as a function of the in-plane lattice parameters interpolating between the experimental values of $FeCl_3$ and $FeBr_3$, $a = 6.05$ and 6.40 Å, respectively. As a benchmark to our methodology, we have obtained J_1 and J_2 values in good agreement with those reported for $FeCl_3$ via inelastic neutron scattering [11] giving rise to a spiral spin liquid state with $|J_1/J_2| \approx 4$.

To reproduce the high-spin configuration and J_1/J_2 found experimentally in $FeCl_3$ and $FeBr_3$, on-site Coulomb interactions must be included in DFT. We found that $U_{dd} = 7.0$, $U_{pp} = 0.5$, and $U_{pp} = 3.5$ eV were required in the Fe, Cl, and Br atoms, respectively, to obtain the SSL state in $FeCl_3$ and FM state in $FeBr_3$ (Supplemental Figs. S2, 3) [14]. We verified that this trend was robust against changes in the local interactions and the inclusion of spin-orbit coupling [14]. The larger value of p-orbital potential in $FeBr_3$ was necessary for establishing the experimentally observed FM state within the honeycomb planes. Smaller values of U_{pp} would lead to a much larger J_2 and establish an AFM (Néel) state within the honeycomb planes of $FeBr_3$ due to the more covalent nature of Fe-Br bonds compared to Fe-Cl bonds. Note that the intralayer correlations are FM within an A-type AFM order [Fig. 3(g)] consistent with the positive Θ_W observed in $FeBr_3$ [Fig. 2(f)]. Our calculations are performed on a 2D lattice without considering the interlayer coupling J_c that eventually establishes the 3D A-type AFM order in $FeBr_3$ (SI).

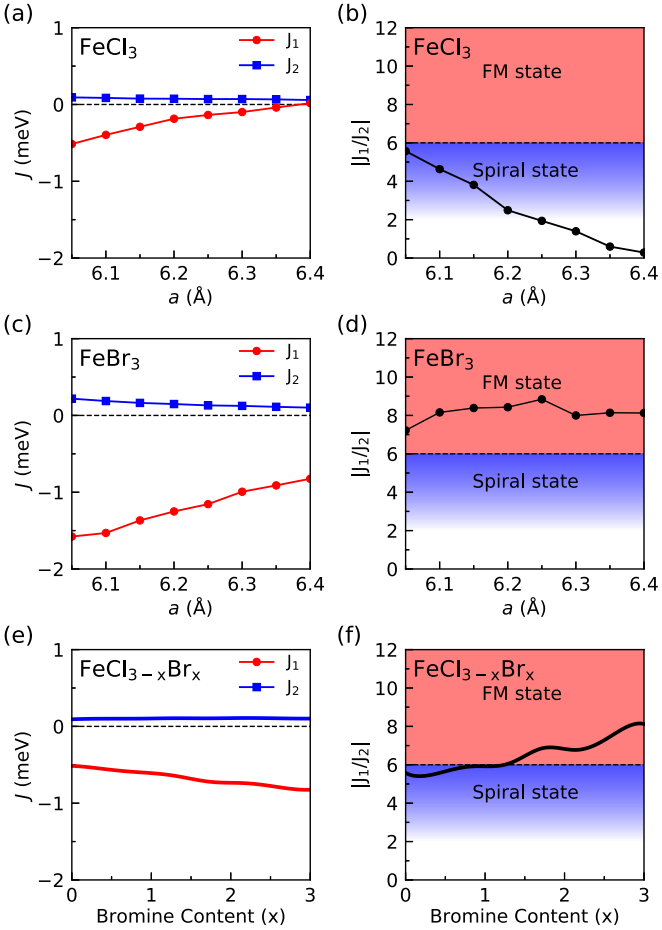

FIG. 4. (a) NN (J_1) and NNN (J_2) coupling constants computed from first principles and plotted as a function of in-plane lattice parameter a in stoichiometric $FeCl_3$. The left and right boundaries of the x axes in panels (a)–(d) correspond to the a axis of $FeCl_3$ and $FeBr_3$, respectively. (b) The ratio $|J_1/J_2|$ plotted as a function of a. (c),(d) Same as in (a),(b) but for the stoichimetric $FeBr_3$. (e) J_1 and J_2 traced as a function of bromine content x in $FeCl_{3-x}Br_x$ using virtual lattice approximation. (f) $|J_1/J_2|$ as a function of x.

Figures 4(a)–4(d) show the evolution of J_1, J_2 and $|J_1/J_2|$ as a function of the in-plane lattice parameters of $FeCl_3$ ($a = 6.05$ Å) and $FeBr_3$ ($a = 6.40$ Å). We observe that, for stoichiometric $FeCl_3$, an increase in the lattice parameter dramatically impacts $|J_1|$ unlike $|J_2|$ [Fig. 4(a)], while the system remains in the spiral state [Fig. 4(b)]. In contrast, the stoichiometric $FeBr_3$ remains in the FM state for all lattice parameter values due to a much larger $|J_1|$ [Figs. 4(c) and 4(d)]. The dashed lines in Figs. 4(b) and 4(d) mark the critical value $|J_1/J_2| = 2Z = 6$ for the theoretical transition from the SSL to FM/Néel state [6–8]. To account for the alloys $FeCl_{3-x}Br_x$, we use a virtual crystal approximation (SI) to estimate J_1 and J_2 as a function of x based on the alloy-dependent lattice constant [Figs. 4(e) and 4(f)]. Within this approximation, doping $FeCl_3$ with Br drives the 2D system from the spiral to the FM phase, as observed experimentally.

The theoretical phase diagram in Fig. 4(f) shows a change of the ground state from SSL to FM at $x = 0.8$ in 2D layers of $FeCl_{3-x}Br_x$. This is consistent with the experimental data in Figs. 2(e), 2(f), and 2(h) that show a jump in T_N, sign change in Θ_W, and MM transition at $x > 0.08$. However, the theoretically predicted critical doping $x_c = 0.8$ differs from the experimentally observed $x_c = 0.08$. Such a difference likely stems from limitations of the DFT methodology that neglects the impact of disorder on exchange interactions. Spin liquid phases (e.g., SSL) are particularly sensitive to disorder [7,8,30,31] and thus it is conceivable that the alloying procedure would change the critical doping via disorder effects that are not captured in the pristine-limit DFT calculations.

III. CONCLUSION

To summarize, we demonstrated a change of the magnetic ground state by tuning the halide composition in the frustrated VdW system $FeCl_{3-x}Br_x$. Our results demonstrate the application of halide engineering in tuning the J_1/J_2 ratio of the underlying frustrated honeycomb spin model, in particular crossing the critical point of the spin spiral liquid at $x_c = 0.08$. The transition driven by the halide composition from a spiral to FM state was demonstrated with magnetometry measurements and the ground states were determined by neutron scattering results presented here for $FeBr_3$ and elsewhere [12] for $FeCl_3$. Our theoretical calculations further show that the transition from the spiral to FM state is driven by competing magnetic exchanges with a sizable contribution from the p-orbital correlations of halides. Our results establish a strategy for engineering frustrated VdW magnetic materials by exploiting a continuous parameter realized by mixed halide chemistry.

ACKNOWLEDGMENTS

The work at Boston College was supported by the National Science Foundation under Award No. DMR-2203512. J.L.L. and A.F. acknowledge the computational resources provided by the Aalto Science-IT project, the financial support from the Academy of Finland Projects No. 331342, No. 336243, and No. 349696, and the Jane and Aatos Erkko Foundation. S.N. was supported by the Quantum Science Center (QSC), a National Quantum Information Science Research Center of the U.S. Department of Energy (DOE). E.F. and H.B.C. were supported by the U.S. Department of Energy (DOE), Office of Science, Office of Basic Energy Sciences, Early Career Research Program Award No. KC0402020, under Contract No. DE-AC05-00OR22725. A portion of this research used resources at the High Flux Isotope Reactor, a DOE Office of Science User Facility operated by the Oak Ridge National Laboratory.

[1] L. Savary and L. Balents, Rep. Prog. Phys. **80**, 016502 (2017).

[2] X.-P. Yao, J. Q. Liu, C.-J. Huang, X. Wang, and G. Chen, Front. Phys. **16**, 53303 (2021).

[3] J. Villain, R. Bidaux, J.-P. Carton, and R. Conte, J. Phys. **41**, 1263 (1980).
[4] V. Fritsch, J. Hemberger, N. Büttgen, E.-W. Scheidt, H.-A. Krug von Nidda, A. Loidl, and V. Tsurkan, Phys. Rev. Lett. **92**, 116401 (2004).
[5] G. J. MacDougall, D. Gout, J. L. Zarestky, G. Ehlers, A. Podlesnyak, M. A. McGuire, D. Mandrus, and S. E. Nagler, Proc. Natl. Acad. Sci. USA **108**, 15693 (2011).
[6] S. Gao, O. Zaharko, V. Tsurkan, Y. Su, J. S. White, G. S. Tucker, B. Roessli, F. Bourdarot, R. Sibille, D. Chernyshov, T. Fennell, A. Loidl, and C. Rüegg, Nat. Phys. **13**, 157 (2017).
[7] D. Bergman, J. Alicea, E. Gull, S. Trebst, and L. Balents, Nat. Phys. **3**, 487 (2007).
[8] N. Niggemann, M. Hering, and J. Reuther, J. Phys.: Condens. Matter **32**, 024001 (2020).
[9] A. Mulder, R. Ganesh, L. Capriotti, and A. Paramekanti, Phys. Rev. B **81**, 214419 (2010).
[10] H. Zhang and C. A. Lamas, Phys. Rev. B **87**, 024415 (2013).
[11] S. Gao, M. A. McGuire, Y. Liu, D. L. Abernathy, C. d. Cruz, M. Frontzek, M. B. Stone, and A. D. Christianson, Phys. Rev. Lett. **128**, 227201 (2022).
[12] J. W. Cable, M. K. Wilkinson, E. O. Wollan, and W. C. Koehler, Phys. Rev. **127**, 714 (1962).
[13] E. R. Jones, O. B. Morton, L. Cathey, T. Auel, and E. L. Amma, J. Chem. Phys. **50**, 4755 (1969).
[14] See Supplemental Material at http://link.aps.org/supplemental/10.1103/PhysRevMaterials.7.064401 for additional explanation of experimental methods, Curie-Weiss fits, and neutron diffraction analysis.
[15] H. Cao, B. C. Chakoumakos, K. M. Andrews, Y. Wu, R. A. Riedel, J. Hodges, W. Zhou, R. Gregory, B. Haberl, J. Molaison, and G. W. Lynn, Crystals **9**, 5 (2019).
[16] B. C. Chakoumakos, H. Cao, F. Ye, A. D. Stoica, M. Popovici, M. Sundaram, W. Zhou, J. S. Hicks, G. W. Lynn, and R. A. Riedel, J. Appl. Crystallogr. **44**, 655 (2011).
[17] O. Arnold *et al.*, Nucl. Instrum. Methods Phys. Res., Sect. A **764**, 156 (2014).
[18] J. Perez-Mato, S. Gallego, E. Tasci, L. Elcoro, G. de la Flor, and M. Aroyo, Annu. Rev. Mater. Res. **45**, 217 (2015).
[19] J. Rodríguez-Carvajal, Phys. B: Condens. Matter **192**, 55 (1993).
[20] The Elk Code, http://elk.sourceforge.net.
[21] P. Gopal, M. Fornari, S. Curtarolo, L. A. Agapito, L. S. I. Liyanage, and M. B. Nardelli, Phys. Rev. B **91**, 245202 (2015).
[22] R. M. Sheetz, I. Ponomareva, E. Richter, A. N. Andriotis, and M. Menon, Phys. Rev. B **80**, 195314 (2009).
[23] L. A. Agapito, S. Curtarolo, and M. Buongiorno Nardelli, Phys. Rev. X **5**, 011006 (2015).
[24] K. J. May and A. M. Kolpak, Phys. Rev. B **101**, 165117 (2020).
[25] M. Abramchuk, S. Jaszewski, K. R. Metz, G. B. Osterhoudt, Y. Wang, K. S. Burch, and F. Tafti, Adv. Mater. **30**, 1801325 (2018).
[26] T. A. Tartaglia, J. N. Tang, J. L. Lado, F. Bahrami, M. Abramchuk, G. T. McCandless, M. C. Doyle, K. S. Burch, Y. Ran, J. Y. Chan, and F. Tafti, Sci. Adv. **6**, eabb9379 (2020).
[27] J. W. Cable, M. K. Wilkinson, and E. O. Wollan, J. Phys. Chem. Solids **19**, 29 (1961).
[28] J. B. Goodenough, J. Phys. Chem. Solids **6**, 287 (1958).
[29] J. Kanamori, J. Phys. Chem. Solids **10**, 87 (1959).
[30] W.-H. Kao, J. Knolle, G. B. Halász, R. Moessner, and N. B. Perkins, Phys. Rev. X **11**, 011034 (2021).
[31] V. Dantas and E. C. Andrade, Phys. Rev. Lett. **129**, 037204 (2022).